JACS
JOURNAL OF THE AMERICAN CHEMICAL SOCIETY
pubs.acs.org/JACS
Article

Controlling the Shape Anisotropy of Monoclinic $Nb_{12}O_{29}$ Nanocrystals Enables Tunable Electrochromic Spectral Range

Hsin-Che Lu,[§] Naman Katyal,[§] Graeme Henkelman,* and Delia J. Milliron*

Cite This: J. Am. Chem. Soc. 2021, 143, 15745−15755
Read Online

ACCESS | Metrics & More | Article Recommendations | Supporting Information

ABSTRACT: Electrochromic smart windows that modulate the solar transmittance in a wide and selective spectral range can optimize building energy efficiency. However, for conventional materials such as bulk transition metal oxides, the electrochromic spectral range is constrained by their crystal structure with limited tunability. Herein, we report a method to control the shape anisotropy of monoclinic $Nb_{12}O_{29}$ nanocrystals and obtain a tunable electrochromic spectral range. We demonstrate the synthesis of monoclinic $Nb_{12}O_{29}$ nanorods (NRs), extending one-dimensionally along the b direction, and monoclinic $Nb_{12}O_{29}$ nanoplatelets (NPLs), extending two-dimensionally along the b and c directions. Upon electrochemical reduction accompanied by Li insertion, the NR films show increasing absorbance mostly in the near infrared region. In contrast, the NPL films show increasing absorbance in the near infrared region first followed by increasing absorbance in both visible and near infrared regions. To elucidate the influence of shape anisotropy, we used density functional theory to construct the lithiated structures of monoclinic $Nb_{12}O_{29}$ and in these structures we identified the presence of square planar sites and crystallographic shear sites for Li insertion. By calculating the theoretical spectra of the lithiated structures, we demonstrate that the Li insertion into the square planar sites results in absorption in the near infrared region in both NRs and NPLs due to their extension in the b direction, while the subsequent insertion of Li into the crystallographic shear sites leads to absorption in both visible and near infrared regions, which only occurs in NPLs due to their extension in the c direction.

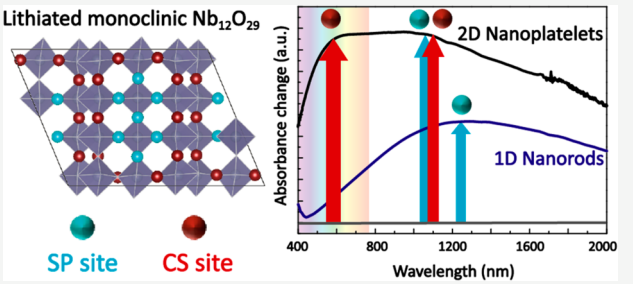

INTRODUCTION

Electrochromic smart windows are designed to mitigate building energy consumption by modulating the solar transmittance under the stimulus of an external potential.[1,2] Upon switching, electrochromic materials, which modulate the solar spectrum in a wide and selective spectral region, can help the windows reach better efficiency under various weather conditions.[3−6] For instance, materials that selectively block only the near infrared (NIR) light can maintain moderate solar transmittance change without compromising the indoor brightness. Bulk transition metal oxides, including tungsten(VI) oxides (WO_{3-x}), niobium(V) oxides (Nb_2O_{5-x}), etc., have been considered as smart window materials due to their stability and wide spectral range.[2] However, limited tunability was reported regarding selective modulation since the electrochromic spectral range of these oxides is constrained by their crystal structure.[7,8] This is because in transition metal oxides, the polaronic mechanism that governs the electrochromic properties is a faradaic process involving the redox of the metal ions accompanied by Li insertion/deinsertion,[9−11] and the resulting optical change is dominated by the local structure surrounding the sites (or cavities) where the Li resides.[12,13] In this regard, we sought to determine whether mesoscale structure, specifically the size and shape of nanocrystals, can influence the spectral range of electrochromic modulation in a transmission metal oxide material, allowing tunability beyond the optical response determined by the Li insertion sites in the crystal structure.

Transition metal oxide nanocrystals have drawn considerable attention as candidate materials for electrochromic smart windows due to their rich tunability through structural control.[2] By applying a colloidal approach, several structural features of the nanocrystals can be precisely controlled, including crystal phase,[4] particle size,[14] morphology,[15] aliovalent dopant concentration,[16] etc. At an atomic level, it was reported for WO_{3-x} bulk films and nanocrystals that the local structure of the Li insertion sites has an influence on their coloration efficiency and stability.[13,17,18] Moreover, it was shown that engineering the surface facets of WO_{3-x} nanocrystals by structural control can be used as a method to optimize several electrochromic properties.[18] Nevertheless, no significant change in the electrochromic spectral range was

Received: July 3, 2021
Published: September 14, 2021

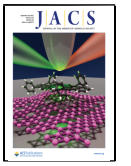

https://doi.org/10.1021/jacs.1c06901
J. Am. Chem. Soc. 2021, 143, 15745−15755

observed by engineering the Li insertion sites in these materials where a polaronic mechanism dominates. By contrast, in plasmonic transition metal oxide nanocrystals, nanocrystal shape has significant impact on the spectral range of electrochromic response in the nanocrystals.[15,19,20] During electrochemical reduction, the injected electrons accompanying Li insertion in metal oxides can be localized to a varying extent. In plasmonic metal oxides the added electrons tend to be delocalized, while in polaronic metal oxides they have been described as localized to a varying degree on the transition metal ions near the inserted Li. Establishing mechanistic connections between spectral response and the extent of charge localization may therefore offer an intriguing pathway to enable more spectral tunability in polaronic metal oxides. On the other hand, previous references have reported variations in the electrochromic spectral range of polaronic-dominated niobium(V) oxides in different phases and compositions.[21,22] We have studied the synthesis and electrochromic properties of anisotropic Nb_2O_{5-x} nanocrystals in different phases.[4,23] Among them, the anisotropic nanocrystals of orthorhombic phase show modulation mostly in the NIR region, while in bulk films of orthorhombic Nb_2O_{5-x}, the modulation usually occurs in both NIR and visible regions.[8,24] Despite the spectral difference we observed by employing nanocrystals, the mechanisms for nanocrystal size and shape impacting the electrochromic spectral range of niobium(V) oxides have remained unclear.

Most recently, niobium(V) oxides with crystallographic shears, known as the Wadsley−Roth phase, have been widely explored as electrodes in Li-ion batteries.[25] In Wadsley−Roth crystals, it is believed there are two different local structures governing the Li insertion kinetics. The blocks of vertex-shared octahedra, referred to as the ReO_3 blocks, offer ordered channels to facilitate the one-dimensional diffusion of Li ions,[26,27] whereas the edge-shared octahedra connecting the ReO_3 blocks, known as the crystallographic shears, provide a large amount of Li insertion sites and structural rigidity.[26,28] To date, studies on the Wadsley−Roth crystals are mostly based on microparticles of PNb_9O_{25}, $W_8Nb_{18}O_{69}$, $TiNb_2O_7$, Nb_2O_5, $Nb_{12}O_{29}$, etc.[25−30] Concurrently, both experimental and theoretical efforts have been made to investigate the structure-dependent Li insertion in these microparticles.

Alternatively, we have reported a colloidal route that produces anisotropic monoclinic $Nb_{12}O_{29}$ nanoplatelets (NPLs), a nanoscale Wadsley−Roth crystal extending two-dimensionally only along the b and c diretions.[4] In monoclinic $Nb_{12}O_{29}$ (Figure 1), the crystal structure is composed of 4 × 3 ReO_3 blocks (within the red outlines) connected to the adjacent blocks by crystallographic shears (frame of the red outlines). In each 4 × 3 block, the two Nb^{4+} ions contribute to the metallic conduction and antiferromagnetic order in monoclinic $Nb_{12}O_{29}$.[31,32] In this crystal structure, it was reported that the niobium sites surrounded by different local structures contribute differently to the overall niobium density of states,[28,32] implying a site-dependent electrochromic response. During progressive reduction, NPL films exhibit dual-mode modulation by first absorbing strongly in the NIR region and, at more reductive potentials, absorbing in both visible and NIR regions.[4] The independent control of visible and NIR transmittances was also reported in other nanocrystal systems but has not been observed in Nb_2O_{5-x} films.[33−36] Compared to the other electrochromic Nb_2O_{5-x} films, the NPL films show much higher coloration efficiency ranging

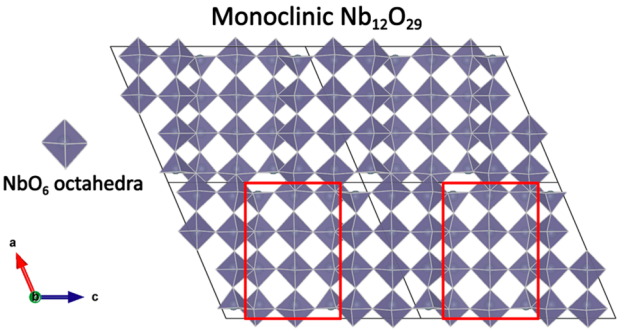

Figure 1. Crystal structure of monoclinic $Nb_{12}O_{29}$ with unit cell framed in black outline. 4 × 3 blocks of vertex-shared NbO_6 octahedra (ReO_3 blocks) are framed in red outlines. Along the b direction, each 4 × 3 block is connected to the next block by vertex-shared octahedra. Extension along the a and c directions shows blocks connecting to adjacent blocks by edge-shared octahedra (crystallographic shears).

from 70 to 185 cm^2/C across both visible and NIR regions.[4] These favorable electrochromic properties motivate us to investigate the mechanistic connections between the anisotropic crystal structure and crystallite shape and the electrochromic response of monoclinic $Nb_{12}O_{29}$ nanocrystals. Herein, we synthesize different morphologies of these intriguing nanocrystals to examine what role the nanocrystal shape might play in their electrochromic properties.

In this article, we report a new synthetic method that enables the colloidal synthesis of two anisotropic nanocrystals, one-dimensional monoclinic $Nb_{12}O_{29}$ nanorods (NRs) and two-dimensional monoclinic $Nb_{12}O_{29}$ nanoplatelets (NPLs). We have systematically investigated the interplay of the shape anisotropy in these two nanocrystals and their electrochromic spectral range by both experimental and theoretical approaches. It was revealed that the presence of the two-dimensional ordered structure in NPLs gives rise to an additional electrochromic mode compared to the single-mode response in NRs. Using density functional theory (DFT), we constructed the lithiated structures of monoclinic $Nb_{12}O_{29}$ and identified the presence of square planar and crystallographic shear sites for Li insertion. The calculated spectra of lithiated monoclinic $Nb_{12}O_{29}$ structures were used to investigate the corresponding electrochromic response due to lithiation occurring in each of the two sites. The NPLs are rich in both sites due to their two-dimensional structure, producing their dual-mode response, while in NRs lithiation is constrained to the square planar sites, resulting in their single-mode response. DFT calculations suggest that the extent of charge localization is limited in NRs where electrons are mostly delocalized, while in NPLs we observed a higher degree of charge localization during electrochemical reduction. Overall, we show that by controlling the shape anisotropy of monoclinic $Nb_{12}O_{29}$ nanocrystals, their electrochromic spectral range can be effectively tuned, aided by changes in the local structure surrounding the Li insertion sites.

EXPERIMENTAL SECTION

Materials. Oleic acid (90%), octadecene (90%), tetraethylene glycol dimethyl ether (TG, >99%), *N*,*N*-dimethylformamide (DMF, anhydrous 99.8%), nitrosonium tetrafluoroborate ($NOBF_4$, 95%), acetone (>99.5%), isopropanol (>99.5%), and hexane (>99%) were purchased from Sigma-Aldrich. Lithium bis(trifluoromethanesulfonyl)imide (Li-TFSI, HQ-115) was purchased from 3M. Ammonium niobium(V) oxalate hydrate (ANO, NH_4[NbO-

https://doi.org/10.1021/jacs.1c06901
J. Am. Chem. Soc. 2021, 143, 15745−15755

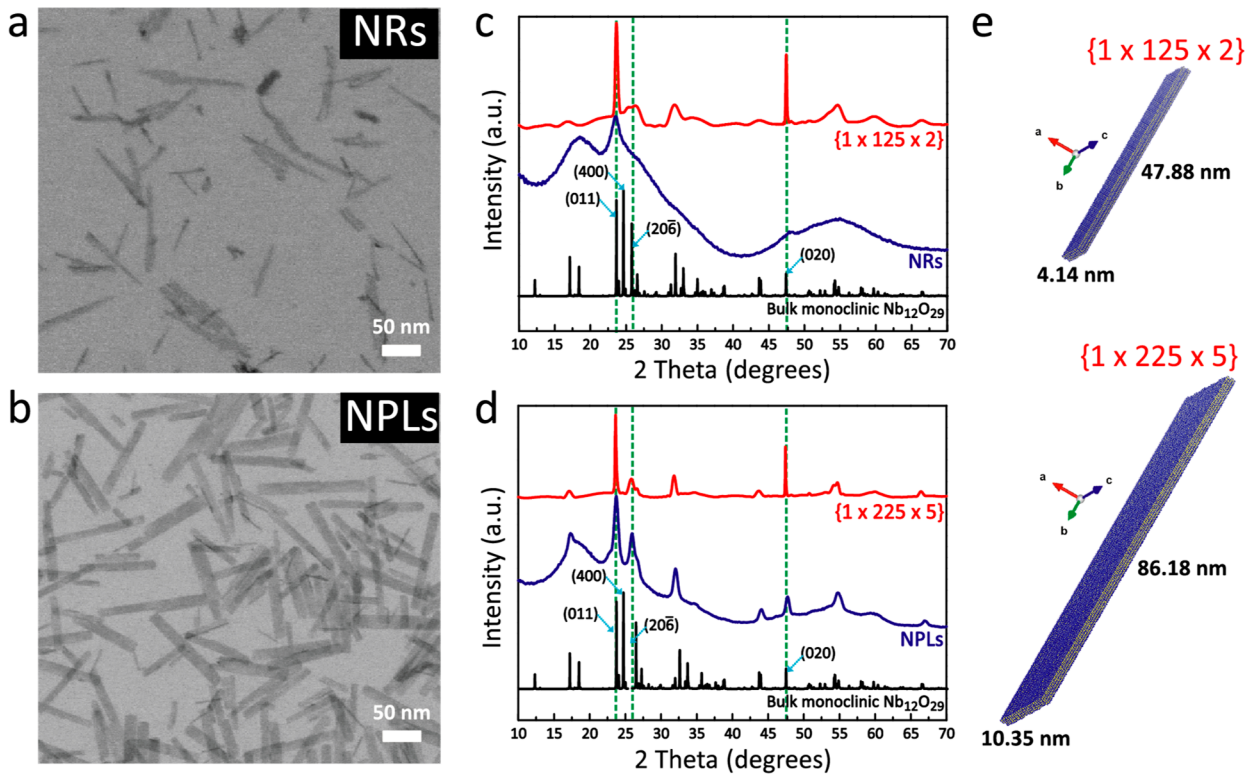

Figure 2. (a, b) Morphological characterization of monoclinic $Nb_{12}O_{29}$ NRs and NPLs using bright-field STEM imaging. (c, d) Structural characterization of monoclinic $Nb_{12}O_{29}$ NRs and NPLs using experimental XRD patterns (blue) and calculated XRD patterns (red) based on {1 × 125 × 2} and {1 × 225 × 5} supercells of monoclinic $Nb_{12}O_{29}$, along with reference pattern (black) of bulk monoclinic $Nb_{12}O_{29}$ crystals. (e) Atomistic models of {1 × 125 × 2} and {1 × 225 × 5} supercells with lateral size matching the average lateral size of NRs and NPLs.

$(C_2O_4)_2(H_2O)_2]\cdot(H_2O)_n$) was provided by Companhia Brasileira de Metalurgia e Mineração (CBMM). Indium tin oxide (ITO)-coated glass substrates (20 Ω/sq) were purchased from Thin Film Devices. Oleic acid and octadecene were heated at 120 °C under vacuum then stored in a N_2 glovebox before use.

Nanocrystal Synthesis. All reactions were performed under N_2 environment on a Schlenk line. In a typical synthesis for both NRs and NPLs, 1.25 g of ANO was mixed with 11.3 g of oleic acid in a three-neck flask and then purged with N_2. The reaction mixture was degassed at 120 °C under vacuum for 30 min, and subsequently the mixture was switched back to N_2 environment and heated at a rate of 8 °C/min to either 240 or 280 °C for the synthesis of NRs or NPLs, respectively. After 1 h of heating at the designated temperature, the reaction mixture was rapidly cooled to room temperature. During synthesis, the reaction mixture appeared as a white and opaque solution with ANO dispersed in the solution. To purify the reaction mixture containing nanocrystals, unreacted ANO, and oleic acid, a washing procedure using hexane as solvent for the dispersion of nanocrystals and isopropanol as antisolvent for flocculation was repeated 3 times. Thereafter, the nanocrystal pellet was redispersed in hexane at a concentration of 30 mg/mL, denoted as ligand-capped nanocrystal dispersion or the as-synthesized nanocrystals and was used throughout the characterization. Aliquots of the nanocrystal synthesis were collected by extracting 500 μL of reaction mixture during the synthesis at various temperatures. Each aliquot was washed just as the nanocrystal dispersion in the typical synthesis. Similar synthesis was performed following the exact procedure except using 10.09 g of octadecene instead of oleic acid to investigate the solvent effect in this synthesis.

Electron Microscopy Imaging. 10 μL of nanocrystal dispersion in hexane was dropped onto carbon-coated copper grids (400 mesh, Ted Pella) and dried overnight in vacuum before analysis. Nanocrystal films were fabricated on Si substrates for imaging. A Hitachi S5500 microscope was operated in scanning electron microscopy (SEM) and scanning transmission electron microscopy (STEM) modes.

X-ray Diffraction (XRD) Analysis. The nanocrystal dispersion was precipitated by adding an excess amount of ethanol, dried, mixed with mineral oil, then mounted on a cryoloop (Hampton Research) for measurement. The XRD pattern was collected on a Rigaku R-Axis Spider equipped with a 1.54 Å Cu Kα radiation. XRD patterns of several hypothetical nanostructures of monoclinic $Nb_{12}O_{29}$ were calculated by using the Debye scattering formula, in which

$$I(q) = \sum_a \sum_b f_a f_b \frac{\sin(q r_{ab})}{q r_{ab}}$$

where $I(q)$ is the scattering intensity, $q = 4\pi \sin\theta/\lambda$ is the scattering vector at half angle θ, and λ is the wavelength of the X-rays. r_{ab} is the distance between atoms a and b that scatter the incident X-rays, and f_a and f_b are their scattering form factors.[37] A crystal visualization program, VESTA,[38] was used to generate the coordinates of the atoms in the hypothetical nanostructures, and the $I(q)$ is the sum of scattering from every individual pair of atoms. Hypothetical nanostructures of monoclinic $Nb_{12}O_{29}$ were made and named as {a × b × c} supercells, meaning the numbers of unit cells repeated in the three crystallographic directions.

Fourier Transform Infrared (FT-IR) Spectroscopy. Nanocrystal dispersions and aliquots collected during synthesis were drop-casted onto Si substrates and dried before measurement. FT-IR spectra were collected by using a Bruker Vertex 70 FTIR at 4 cm^{-1} resolution.

Spectroelectrochemical Measurement. Spectroelectrochemical properties of the nanocrystal films were measured in an Ar glovebox using a Bio-logic VMP3 potentiostat to apply different electrochemical techniques and an ASD Quality Spec Pro spectrometer to collect the optical change concurrently. In a homemade electrochemical cell, the nanocrystal films were used as the working electrode, a Li foil acted as both counter and reference

https://doi.org/10.1021/jacs.1c06901
J. Am. Chem. Soc. 2021, 143, 15745−15755

electrodes, and 1 M Li-TFSI in TG was the electrolyte (1 M Li-TFSI/TG). Upon immersing the nanocrystal films into the electrolyte, 2.901 and 3.044 V (vs Li/Li^+) were recorded as the open-circuited potential (OCP) for the NR and NPL films, respectively.

DFT Calculations. All electronic energies and forces in this work were calculated using the DFT approach using Perdew–Burke–Ernzerhof (PBE) exchange–correlational functional approximation in the Vienna ab initio simulation package (VASP).[39,40] A detailed explanation of the computational techniques is provided in the Supporting Information. The electronic density of states on niobium sites in the monoclinic $Nb_{12}O_{29}$ and lithiated $Nb_{12}O_{29}$ structures was extracted from single-point calculations and plotted using the Pymatgen package.[41] Theoretical ultraviolet–visible (UV–vis) spectra for $Nb_{12}O_{29}$ and the lithiated structures were calculated using the independent particle approximation.[42] Bader electronic charge analysis was done using code maintained by the Henkelman group.[43]

RESULTS AND DISCUSSION

Morphological and Structural Characterizations. Colloidal synthesis of the nanocrystals was carried out by heating the niobium(V) precursor, ANO, in oleic acid at two different temperatures (240 and 280 °C). After purification, the morphology of the as-synthesized nanocrystals was characterized by STEM imaging. The synthesis at 240 °C produces one-dimensional nanocrystals with smaller lateral size (Figure 2a, named as nanorods (NRs)) and at 280 °C produces two-dimensional nanocrystals with larger lateral size (Figure 2b, named as nanoplatelets (NPLs)). In Figure S1, the size distribution histograms collected from the STEM imaging of NRs and NPLs show their average size in both long and short axes. In comparison with our previous publication on the synthesis of monoclinic $Nb_{12}O_{29}$ NPLs using $NbCl_5$ as the precursor,[4] the NPLs presented here have similar lateral size, while the lateral size of the one-dimensional NRs is very thin in the short axis, which is similar to previously reported Nb_2O_5 nanocrystals in pseudohexagonal and orthorhombic phases.[23,44]

The crystal structures of the NRs and NPLs were investigated by both experimental and calculated XRD patterns (Figure 2c and Figure 2d). In the experimental XRD pattern of the NRs (Figure 2c), the only noticeable peak that aligns with bulk monoclinic $Nb_{12}O_{29}$ is the (011) reflection, while the (020) reflection in NRs is relatively weak and broadened. Compared to the noticeable peaks commonly seen in the patterns of bulk crystals, the broadened diffraction pattern of NRs indicates that the NRs share some structural similarity with monoclinic $Nb_{12}O_{29}$ but with most structural motifs remain disordered. As for the experimental pattern of NPLs (Figure 2d), most reflections from bulk monoclinic $Nb_{12}O_{29}$ can be identified with a few exceptions, such as the absent (400) reflection. This suggests that the NPLs lack enough ordered structural motifs in certain crystallographic directions to form constructive interference, leading to the missing reflections. Comparison between the patterns of NRs and NPLs implies that since these two patterns are similar at most diffraction angles except that the NPLs show more noticeable peaks, the NRs could be an intermediate product of the more crystalline NPLs during nanocrystal growth. Additionally, in our previous work,[4] we identified materials with similar XRD pattern as NPLs as monolayer monoclinic $Nb_{12}O_{29}$ nanocrystals extending two-dimensionally along the b and c directions, based on comparison of experimental and simulated XRD patterns.

Analysis based on the calculated XRD patterns of various hypothetical structures that resemble the lateral dimension of NRs and NPLs was performed by applying the Debye scattering formula.[45] For this calculation, atomistic models were made by extending the unit cell of monoclinic $Nb_{12}O_{29}$ into different crystallographic directions, denoted as {a × b × c} supercells. Calculations used to identify the direction of the preferential orientation in NRs and NPLs were collected and discussed in Figure S2. We identified that by extension of monoclinic $Nb_{12}O_{29}$ along the b direction first, (011) and (020) reflections arise as the main peaks in the calculated patterns. Calculated pattern based on the {1 × 125 × 2} supercell, which has similar lateral size with the NRs, was compared to the experimental pattern of NRs in Figure 2c. Although the NRs share the (011) reflection with the reference and calculated patterns, they appear to be poorly crystalline monoclinic $Nb_{12}O_{29}$ extending mostly along the b direction. The calculated patterns in Figure S2 further indicate that the extension along the c direction leads to the emergence of several other reflections, such as the $(20\bar{6})$ reflection, which can all be found in the experimental pattern of NPLs. In Figure 2d, the calculated pattern and the lateral size of {1 × 225 × 5} supercell align well with both experimental pattern and the lateral size of NPLs, indicating their two-dimensional extension along the b and c directions of monoclinic $Nb_{12}O_{29}$. The atomistic models of these two supercells for simulating the structure of NRs and NPLs are shown in Figure 2e. In addition to the above calculations, although the direction of the preferential orientation in NRs was identified, the experimental pattern of the NRs still appears to be less crystalline compared to the calculated pattern in Figure 2c. We have performed another series of calculations to show that the (011) and (020) reflections can be broadened if some of the structural motifs in NRs are disordered, as shown in Figure S3 and discussed in Supporting Information.

In conclusion, the calculated XRD patterns suggest that by use of the colloidal synthesis we designed, the growth of monoclinic $Nb_{12}O_{29}$ nanocrystals is along the b direction first with a one-dimensional morphology and at latter stage extends to both b and c directions with a two-dimensional morphology. The NRs can be seen as an intermediate of the NPLs that form at lower temperature (240 °C), whereas the NPLs, being the more crystalline nanocrystals, form at higher temperature (280 °C). Additionally, in Figure 2c and Figure 2d, the (400) reflection is missing in the experimental patterns of both nanocrystals, suggesting that the NRs and NPLs are very thin along the a direction. This hypothesis is verified by the calculated patterns of {1 × 125 × 2} and {1 × 225 × 5} supercells with only single unit cell in the a direction, as well as the experimental evidence on the monolayer thickness of monoclinic $Nb_{12}O_{29}$ NPLs in our previous work.[4]

Synthetic Mechanism. The colloidal synthesis presented here relies on heating the niobium precursor, ANO, in oleic acid to produce monoclinic $Nb_{12}O_{29}$ nanocrystals. In previous reports, ANO was often used as precursor to produce amorphous niobium(V) oxides by various solvothermal methods, and thereafter the amorphous oxides can be crystallized to different phases by a postsynthetic heating at higher temperatures depending on the phase of interest, for example, 400 °C for orthorhombic phase and 800 °C for monoclinic phase.[46–49] To elucidate the mechanistic difference between our synthesis and previous works, we started by performing similar synthesis using the noncoordinating solvent

https://doi.org/10.1021/jacs.1c06901
J. Am. Chem. Soc. 2021, 143, 15745–15755

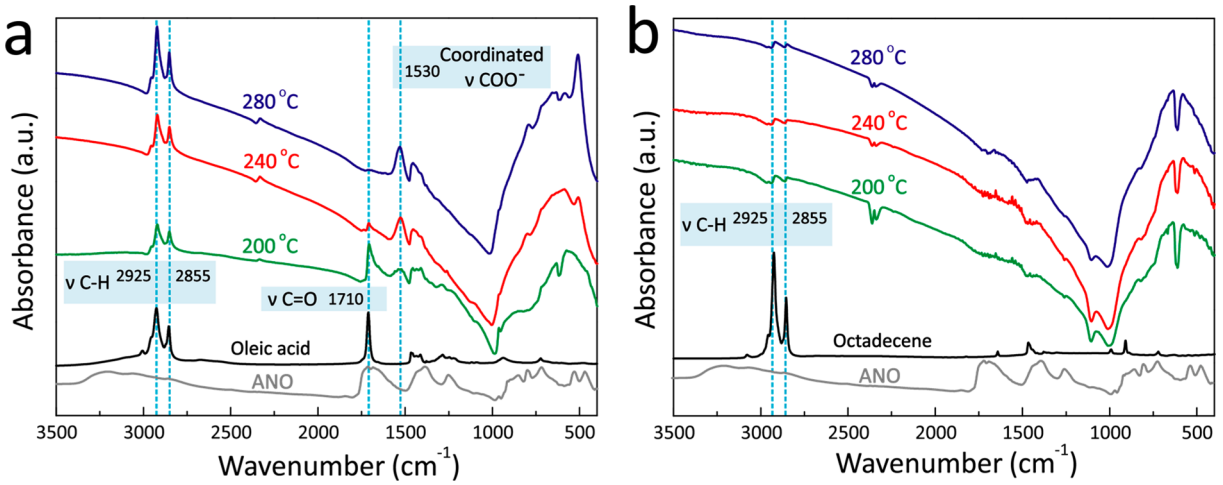

Figure 3. (a, b) FT-IR spectra of ANO, oleic acid, octadecene, and aliquots collected at 200 °C, 240 °C, and 280 °C during the nanocrystal synthesis using oleic acid and octadecene as solvents, respectively. In the spectra, peaks at 2925 and 2855 cm^{-1} correspond to the stretching of C−H bond, the peak at 1710 cm^{-1} corresponds to the stretching of C═O bond, and the peak at 1530 cm^{-1} corresponds to the asymmetric stretching of coordinated COO^- bond.

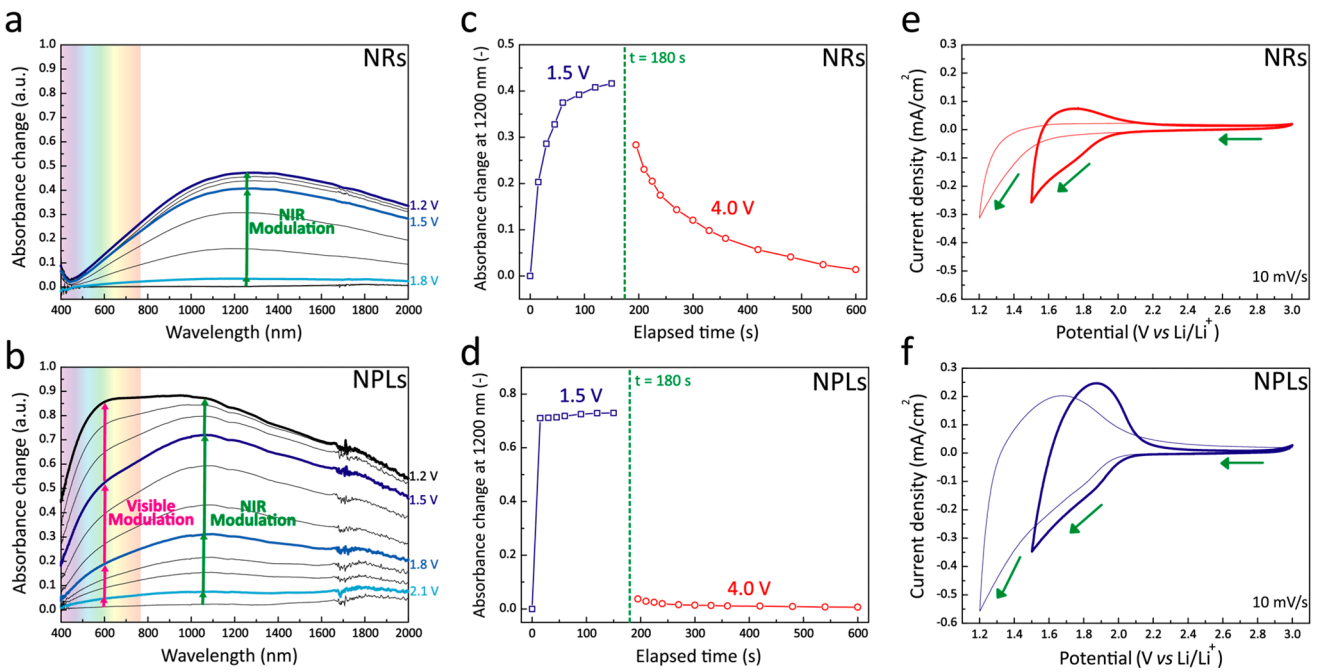

Figure 4. Spectroelectrochemical characterization of the ligand-stripped monoclinic $Nb_{12}O_{29}$ NR and NPL films in 1 M Li-TFSI/TG. (a, b) Absorbance spectra of the nanocrystal films reduced at designated potential (vs Li/Li^+) for 2 min by chronoamperometry. The interval between each spectrum is 0.1 V and the absorbance change is the difference from the OCP state to the reduced states at various potentials. (c, d) Dynamic absorbance change of the nanocrystal films at 1200 nm. The films were first reduced at 1.5 V for 180 s and subsequently oxidized at 4.0 V for 420 s by chronoamperometry. (e, f) Cyclic voltammograms of the nanocrystal films at a scan rate of 10 mV/s. For these measurements, the 5th cycle of the cyclic voltammogram was collected to ensure the films had reached stabilization.

octadecene to investigate the role of coordinating oleic acid. Structurally, synthesis using octadecene produces only amorphous microscale rods with poorly defined morphology at either 240 or 280 °C (Figure S4).

We hypothesized that the coordination between ANO and oleic acid plays an important role in the successful crystallization of monoclinic $Nb_{12}O_{29}$ nanocrystals. As shown in Figure S5, the molecular structures of both oleic acid and octadecene possess rich C−H bonds while the precursor ANO does not so that the FT-IR spectroscopic signature of C−H bonds can be used to identify the presence of solvent molecules on the nanocrystal surface. During the nanocrystal synthesis, we carried out the spectroscopic study of the washed reaction aliquots, meaning only the niobium(V) oxide products and the molecules coordinating on the product surface were probed. From the FT-IR spectra of the aliquots from synthesis in oleic acid (Figure 3a), noticeable peaks from the stretching of C−H bond can be observed in aliquots at different temperatures as the evidence of oleic acid presence even after washing. On the contrary in Figure 3b, the stretching of the C−H bond is considerably weaker in the aliquots from octadecene synthesis, suggesting the absence of

https://doi.org/10.1021/jacs.1c06901
J. Am. Chem. Soc. 2021, 143, 15745−15755

octadecene on the product surface. On the other hand, in Figure 3a, stretching of the C═O bond from oleic acid at 1710 cm^{-1} was observed at the early stage of the synthesis and gradually replaced by another peak at 1530 cm^{-1} along with elevated temperature, which can be attributed to the fingerprint of COO^- bonds coordinating to the oxide surface.[50,51] Structural features of aliquots from the oleic acid synthesis were also probed by Raman spectroscopy (Figure S6). At the early stage of the synthesis (200 °C), the aliquot appears to be a mixture of amorphous niobium oxide and ANO,[52] whereas at 240 and 280 °C we observe Raman spectra with distinctive peaks that resemble the spectra of monoclinic Nb_2O_{5-x}.[53]

The results on synthetic mechanism show that the synthesis of monoclinic $Nb_{12}O_{29}$ nanocrystals using the precursor ANO relies on the coordination of oleic acid during synthesis to regulate and direct the formation of nanocrystals. This method successfully stabilizes the growth of monoclinic $Nb_{12}O_{29}$ in nanoscale along the b direction first, then along both b and c directions, forming NRs and NPLs at different stages. Compared to previous literature, the presented nanocrystal synthesis using our colloidal method produces anisotropic niobium(V) oxide nanocrystals with much smaller dimensions, with better defined morphologies with narrower size distributions and not requiring postsynthetic heating.[46−49]

Spectroelectrochemical Characterization. The monoclinic $Nb_{12}O_{29}$ nanocrystals tested in spectroelectrochemical measurements were first ligand-stripped using $NOBF_4$ to remove the insulating oleic acid ligands on the nanocrystal surface[4,54] and subsequently deposited onto ITO glass substrates for analysis, as detailed in Supporting Information. From the FT-IR spectra of the NR and NPL films (Figure S7), it is clear that the absorbance peaks from the stretching of C−H bond decreased significantly after the ligand-stripping procedure, indicating the successful removal of oleic acid ligands. SEM imaging of the ligand-stripped nanocrystal films shows a smooth surface morphology without severe aggregation (Figure S8).

The spectroelectrochemical characterization of the ligand-stripped nanocrystal films was carried out in a Li-based electrolyte to investigate their electrochromic properties upon Li insertion. In Figure 4, the absorbance spectra are presented as the absorbance change of the nanocrystal films from the spectrum at OCP to the spectrum at designated potential. Upon reduction, starting from 1.8 V, the NR films show absorption centered around 1280 nm in the NIR region and progress toward higher absorbance following lower electrochemical potentials (Figure 4a). Similarly, single-mode electrochromic absorption centered in the NIR region was also reported in other crystalline niobium(V) oxides, in the form of either bulk films or nanoparticles, in contrast to the visible absorption in amorphous niobium(V) oxides.[23,55] The electrochromic absorption of niobium(V) oxides is experimentally known to arise from the reduction of niobium(V) ions followed by the insertion of Li ions,[11] leading to polaronic absorption, similar to the case in some tungsten(VI) oxides.[56,57] However, the absence of calculations based on niobium(V) oxides has limited progress in understanding the electrochromic mechanism following Li insertion.

On the other hand, as shown in Figure 4b, the NPL films absorb primarily in the NIR region first starting from 2.1 to 1.5 V, and thereafter at potentials lower than 1.5 V, a second electrochromic mode that absorbs visible light appears. The sequential dual-mode electrochromic behavior, according to our previous investigation on the electrochromic properties of monoclinic $Nb_{12}O_{29}$ NPLs, can be attributed, respectively, to capacitive charging and Li insertion.[4] At potentials higher than 2.1 V, an even absorption in the NIR region was observed, which can be attributed to the capacitive charging electrochromism instigating the accumulation of delocalized electrons in the conduction band. From 2.1 to 1.5 V, absorption centered around 1060 nm can be observed, and potentials lower than 1.5 V triggered the visible absorption of the NPL films.

When comparing the absorbance spectra of NR and NPL films, it is clear that the intense visible absorption in the NPL films is not reproduced in the NR films. The additional electrochromic mode leading to the absorption in the visible region enables tuning of the electrochromic spectral response in NPLs from NIR-only absorption to absorption in both NIR and visible regions, which is a beneficial feature for smart window operation. As discussed, both NRs and NPLs are structurally similar to monoclinic $Nb_{12}O_{29}$, with NPLs being the one showing more ordered structural motifs in the c direction compared to the poorly crystalline NRs. We propose that at lower insertion level in monoclinic $Nb_{12}O_{29}$ Li ions fill the sites within the ReO_3 blocks and trigger NIR absorption, while at higher insertion level Li ions fill the sites along the crystallographic shears, which are abundant only along the extension in the a and c directions, and thus lead to visible absorption that is not available in the NRs. Similarly, in a previous report on Wadsley−Roth phase PNb_9O_{25}, the insertion of Li ions shows preference of inserting into the relatively opened ReO_3 blocks first and then into the crystallographic shears.[28] The influence of Li insertion on the electrochromic spectral range of monoclinic $Nb_{12}O_{29}$ will be further verified by calculations in the later part of this manuscript.

Aside from spectral control, the kinetics of the monoclinic $Nb_{12}O_{29}$ NR and NPL films were examined by the time required to reach saturated absorbance spectrum in both reduction (coloring) and oxidation (bleaching) processes. In Figure 4c and Figure 4d, we report the dynamic response of the NRs and NPLs, and the whole spectra are presented in Figure S9. Upon initial reduction at 1.5 V (in both Figure 4c and Figure 4d), the NR and NPL films both reach their saturated absorbance change within 60 s. Among these two, the NPL film shows faster coloring response. On the other hand, we observed that the kinetics of the reverse process in these two nanocrystals differ significantly. In Figure 4c, after applying 4.0 V to oxidize the NR film from the reduced state at 1.5 V, it takes roughly 5 min to bleach to the original state of the films, while at the same condition, the NPL film can reach its original state within 60 s (Figure 4d).

We proposed that in monoclinic $Nb_{12}O_{29}$, having ordered arrangement in the structural motifs along the c direction can facilitate the kinetics of Li insertion/deinsertion when compared to their poorly crystalline counterparts. It is generally acknowledged that in niobium(V) oxides, disordered structure in the amorphous phase is detrimental to the kinetics of Li insertion/deinsertion.[58,59] As shown in Figure 1 and consistent with the conclusions from one earlier report,[26] Li ions generally move efficiently in the ordered channel within the ReO_3 blocks along the b direction. The two-dimensional motion along the ac plane can be within the ReO_3 blocks or moving across the crystallographic shears to the ReO_3 blocks.[26]

https://doi.org/10.1021/jacs.1c06901
J. Am. Chem. Soc. 2021, 143, 15745−15755

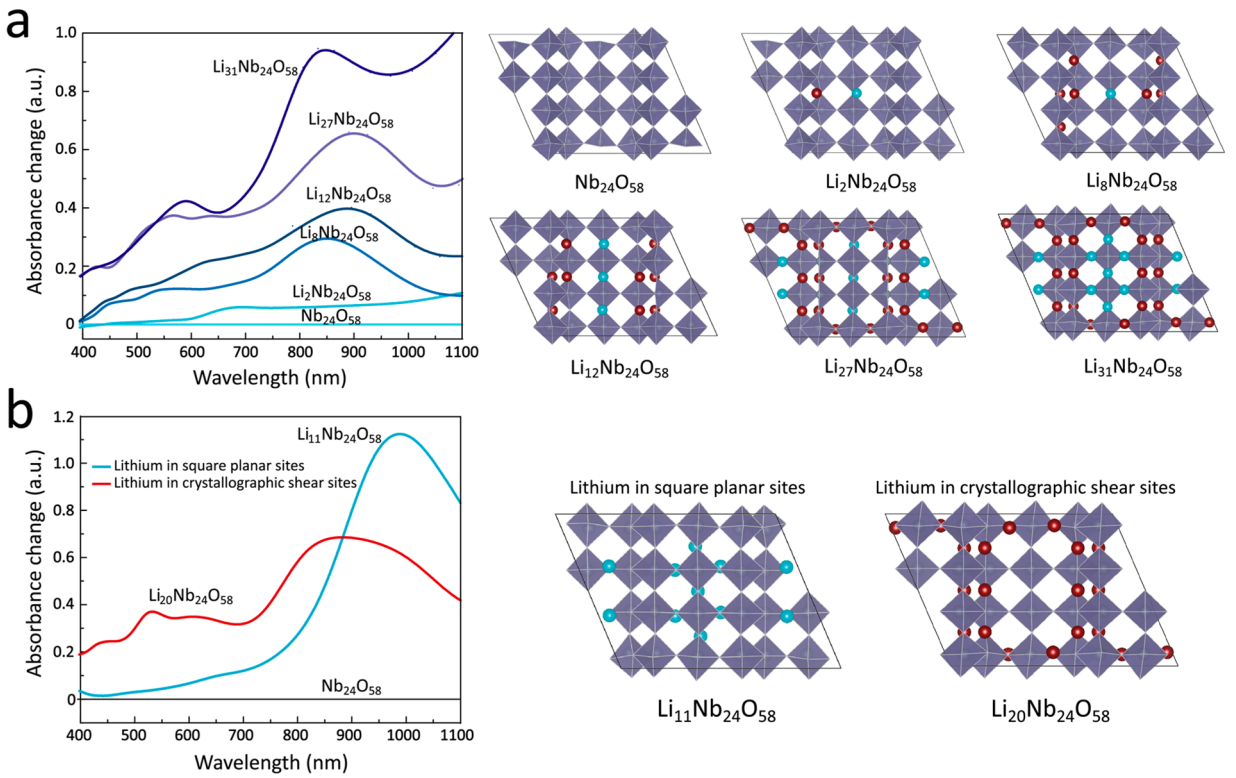

Figure 5. (a) Calculated absorbance spectra for lithiated monoclinic $Nb_{12}O_{29}$ structures relative to the unlithiated monoclinic $Nb_{12}O_{29}$ and the corresponding simulated structures. Color scheme on right: NbO_6 octahedra (blue-gray), Li in square planar sites (cyan), and Li in crystallographic shear sites (dark red). (b) Absorbance spectra for lithiated monoclinic $Nb_{12}O_{29}$ relative to the unlithiated monoclinic $Nb_{12}O_{29}$ with Li only in the crystallographic shear sites or the square planar sites.

We believe that the relatively sluggish kinetics in NRs is the result of having disordered structural motifs in the crystallographic shears, which is verified by their lack of ordered structure in the c direction. Therefore, in NRs, due to potentially larger activation barrier from the disordered structural motifs, it could be difficult to insert and extract Li ions. In the case of NPLs, the kinetics are more rapid, made possible by the more ordered structural motifs along the c direction.

The electrochemical properties of the monoclinic $Nb_{12}O_{29}$ nanocrystal films upon Li insertion were investigated by different electrochemical techniques. The cyclic voltammograms of the NR and NPL films were measured at a scan rate of 10 mV/s in two different potential windows (Figure 4e and Figure 4f). In the cyclic voltammograms of NPL films (Figure 4f), pronounced redox peaks can be observed due to the redox of the niobium(V) ions accompanied by the insertion/deinsertion of Li ions. On the contrary, for the NR film (Figure 4e), similar redox peaks can still be observed but the current density from the oxidation of the film is much smaller than the reduction process. When cycled to lower potential (Figure 4e, from 3.0 to 1.2 V), the NRs films suffered severe degradation and no peak can be observed in the oxidation process, corresponding to their sluggish oxidation kinetics. When using niobium(V) oxides as electrodes for Li ion storage, the amorphous phase is considered to have poor kinetics and often shows an irreversible cyclic voltammogram with weak oxidation peak current,[59] similar to the cyclic voltammograms in Figure 4e. The poorly crystalline nature of NRs produces similar electrochemical behavior as amorphous niobium(V) oxide films, but interestingly, the electrochromic spectral range of these two materials are drastically different since the amorphous films absorb mostly in the visible region. In addition, the electrochemical kinetics and reversibility of the NR and NPL films were investigated by chronoamperometry, as discussed in Figure S10 and Supporting Information.

Overall, we have shown that in NPLs, being the more crystalline material in the c direction compared to NRs, Li insertion alongside the reduction of niobium(V) ions can trigger the electrochromic absorption in the NIR region first and then in both NIR and visible regions with efficient and reversible kinetics. By contrast, the NRs do not allow visible absorption upon Li insertion in the reduction process, and the reversed oxidation kinetics are sluggish and irreversible. Structurally, we reason that the additional sites in NPLs brought by ordering in the c direction facilitate the insertion and deinsertion kinetics and help the NPLs to reach higher insertion level, which triggers visible absorption. To quantify the amount of Li ions stored in the nanocrystal films, we injected a constant current density to the NR and NPL films by chronopotentiometry (Figure S11). When the potential reached 1.5 V, 15.5 and 3.2 Li ions per unit cell of monoclinic $Nb_{12}O_{29}$ were injected in the NPL and NR films, respectively, highlighting the higher Li insertion level in NPLs and potentially indicating multielectron reduction.

Electronic Structure Calculations. Electrochromism of $Nb_{12}O_{29}$ involves insertion of Li ions during the cathodic scan (coloration) and deinsertion of Li ions during the reverse scan (bleaching). Since Li insertion and deinsertion are the driving forces for electrochromism, the changes in the electronic structure should be linked to the absorbance change. Electronic structure calculations have explored the Li insertion

https://doi.org/10.1021/jacs.1c06901
J. Am. Chem. Soc. 2021, 143, 15745−15755

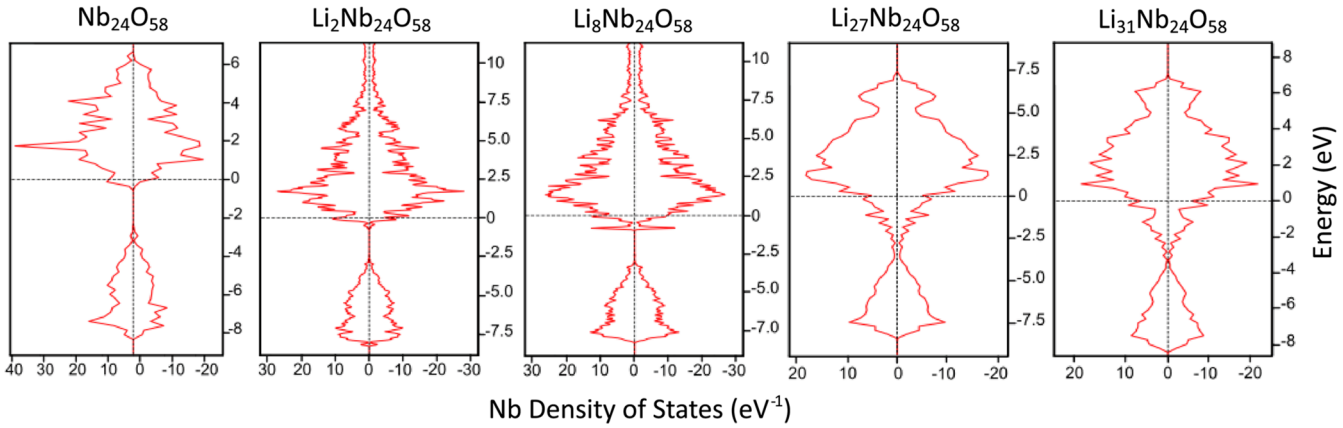

Figure 6. DFT calculated density of states on niobium as a function of Li composition.

in oxides to understand the electrochromic properties. Liang et al. studied the changes in density of states on tungsten sites upon Li insertion in tungsten oxide.[60] Li et al. calculated the relationship between absorption coefficient for the visible to infrared transition and structural changes in $Li_4Ti_5O_{12}$ during the Li insertion/deinsertion process using electronic structure calculations.[61] He et al. also studied the correlated structure evolution to the coloring of Li doped nickel oxides using DFT calculations.[62] In this section, we aimed at applying electronic structure calculations to elucidate the relationship between Li insertion sites and the electrochromic spectral range of monoclinic $Nb_{12}O_{29}$. DFT calculations have been shown to provide an understanding of the geometric and electronic structure of $Nb_{12}O_{29}$.[32,63] Consistent with these previous calculations, we first determined lattice constants of monoclinic $Nb_{12}O_{29}$ (see Table S1 in the Supporting Information) and found them to be in good agreement with experiment. Upon the basis of these optimized structures, we investigated the insertion of Li into $Nb_{12}O_{29}$. Since both the NRs and NPLs have a similar XRD pattern to monoclinic $Nb_{12}O_{29}$, we have assumed that they have similar possible Li insertion sites. Previous work has reported that the electrochemical reduction of monoclinic $Nb_{12}O_{29}$ can host 14.3 Li^+,[30] and our analysis show that there are 15.5 Li insertion sites in $Nb_{12}O_{29}$ or 31 sites in the full unit cell ($Nb_{24}O_{58}$). We identified two distinct sites for Li insertion: crystallographic shear sites in the edge-shared octahedra (or along the crystallographic shears) and square planar sites in the vertex-shared octahedra (ReO_3 blocks). There are 20 shear sites and 11 square planar sites in one unit cell ($Nb_{24}O_{58}$), and we have explored their stepwise lithiation. Figure 5a shows the favorable lithiated structures as a function of Li concentration.

To understand the effect of lithiation in $Nb_{12}O_{29}$, we studied the electronic density of states at the Nb sites. In monoclinic $Nb_{12}O_{29}$, there are two Nb^{4+} and ten Nb^{5+} sites, giving 2 d electrons per formula unit. Gray et al. reported that $Nb_{12}O_{29}$ has only localized electrons at Nb^{4+} sites, whereas Cava et al. reported that one electron is localized on one of Nb^{4+} sites while the other electron is fully delocalized over the unit cell.[31,64−68] Our Bader electronic charge analysis (Table S2 in Supporting Information) reveals that the charge is delocalized on all Nb sites in the unit cell. This result follows the Stoner instability of electronic structure of the Nb^{5+} which was tested by Zandbergen et al.[69] Upon lithiation, the Bader charge analysis shows that the electronic contribution from Li insertion provides a mix of localized and delocalized states on the Nb sites. This is in contrast to similar materials like PNb_9O_{25},[28] where at low Li concentration, electronic states are localized on the Nb sites as distinct paramagnetic spin states but at higher concentrations, the material transforms into a metallic state with delocalized d-states on the Nb sites. To further understand the electronic state of lithiated $Nb_{12}O_{29}$, we separately populated the shear and square planar sites, as shown in Figure 5b. A Bader analysis (Table S2 in Supporting Information) shows that the electrons from Li in crystallographic shear sites are primarily localized on the Nb sites neighboring the inserted Li ions while the electrons from Li in square planar sites are delocalized evenly on all the Nb sites. The findings from Bader analysis also align well with our previous results using X-ray photoelectron spectroscopy (XPS).[4] At lower electrochemical potentials, the reduction of NPLs gives rise to a higher degree of charge localization following Nb^{5+} reduction due to the Li inserting into the crystallographic shear sites, while at higher electrochemical potentials the degree of charge localization is limited since the Li inserts mostly in the square planar sites. The latter situation, giving rise to only NIR absorption, occurs also in NRs where the Li insertion is constrained to the square planar sites. The density of states on Nb sites for the unlithiated and lithiated monoclinic $Nb_{12}O_{29}$ are shown in Figure 6; the presence of electronic states at the Fermi level shows agreement with its experimentally measured metallic state.[69] As expected, lithiation of $Nb_{12}O_{29}$ fills up the unoccupied d-orbitals of Nb.

We believe that the structural difference between NRs and NPLs influences the Li insertion process, which in turn dictates the associated differences in the absorbance spectra, as shown in Figure 5. These calculated absorbance spectra can also be used to explain the qualitative difference in the NR vs NPL experimental absorbance spectra in Figure 4a and Figure 4b. The calculated absorbance spectra show the two regions of importance: lower wavelength in the visible region (550−600 nm) and the NIR region (850−900 nm). For the fully lithiated $Li_{31}Nb_{24}O_{58}$, the absorbance is twice as large in the NIR region as compared to the visible region. In Figure 5b, we see that Li insertion in the square planar sites gives a response only in the NIR region whereas with Li in the shear sites the absorbance is almost equal in the visible and NIR. The stepwise filling of these two sites, in Figure 5a, gives an additive combination of the two spectra.

The calculated absorbance spectra help to explain the different electrochromic response of the NRs and NPLs in Figure 4a and Figure 4b. The absorbance for the NRs

https://doi.org/10.1021/jacs.1c06901
J. Am. Chem. Soc. 2021, 143, 15745−15755

corresponds to Li in the square planar sites adding delocalized electrons on niobium sites, giving rise to a response only in the NIR region. The presence of Li in the square planar site also indicates that Li insertion is unavailable in the crystallographic shear sites, which are dominant along the a and c directions (or the (100) and (001) planes, considering that insertion occurs at the surface) and support the model that NRs are monolayers in the a and c directions. A monolayer along the a and c directions can lead to surface reconstruction and prevent Li insertion into the crystallographic shear sites. Similarly, due to their extension in the b and c directions, the absorbance of the NPLs corresponds to the lithiation in both square planar sites and crystallographic shear sites adding a combination of delocalized and localized electrons on niobium sites, giving rise to the response in both the NIR and visible regions. It is clear that in NPLs, the absorption in visible and NIR regions is controlled by localized electrons and delocalized electrons, respectively. As observed in Figure 4b, the absorbance first builds up in the NIR region and then to the visible region, implying that the square planar sites are filled before the crystallographic shear sites. Simultaneously this transition can be delineated by the changing extent of charge localization following Li insertion, which determines the electrochromic spectral range in monoclinic $Nb_{12}O_{29}$.

CONCLUSIONS

We have demonstrated the synthesis and structural characterization of monoclinic $Nb_{12}O_{29}$ nanocrystals in two different morphologies: the NRs extend one-dimensionally along the b direction, and the NPLs extend two-dimensionally along the b and c directions. This synthesis relies on the coordination of oleic acid during the particle growth to direct the formation of the desired monoclinic $Nb_{12}O_{29}$ phase. Upon electrochemical reduction, the NR films show increasing absorbance mostly in the NIR region. As for the NPL films, dual-mode electrochromism was observed with the first mode absorbing the NIR region and the second mode absorbing both NIR and visible regions. In addition, more reversible electrochemical switching with more rapid kinetics was observed in the NPL films. We attributed the difference in the electrochromic properties of NR and NPL films to the structural difference at the atomic and nanoscale. On the basis of both experimental efforts and DFT calculations, we showed that by having ordered structure in both b and c directions of monoclinic $Nb_{12}O_{29}$, a rich abundance of crystallographic shear sites and square planar sites for Li insertion can be found in the NPLs, while in the NRs, Li insertion is limited to square planar sites, resulting in NIR absorption. Results from Bader analysis indicate that the activation of electrochromic absorption in different spectral regions is determined by the extent of charge localization during Li insertion. In NRs, the insertion sites lie along the b direction only and electrons are mostly delocalized, while in NPLs, electrons added electrochemically can become localized, activating visible absorption that was not observed in NRs. By establishing the principles underlying the electrochromic response of monoclinic $Nb_{12}O_{29}$ in different nanostructures, we have advanced the understanding of niobium(V) oxides and helped to lay the foundation for better design of electrochromic smart windows based on niobium(V) oxide nanocrystals. Specifically, our results demonstrate the methodology of controlling the electrochromic response of niobium(V) oxide nanocrystals by shape anisotropy and the underlying mechanism that can benefit the design of other niobium(V) oxide nanocrystals in smart windows and potentially can be applied to other metal oxide nanocrystals.

ASSOCIATED CONTENT

Supporting Information

The Supporting Information is available free of charge at https://pubs.acs.org/doi/10.1021/jacs.1c06901.

Nanocrystal size distribution histograms; calculated XRD patterns for explaining the orientation direction of NRs and NPLs and the amorphous feature of NRs; SEM images and experimental XRD patterns for octadecene synthesis; molecular structures of ANO, oleic acid, and octadecene; procedure, figure, and discussion of the aliquot study using Raman spectroscopy; procedure for ligand stripping method and the FT-IR spectra of nanocrystals before and after the ligand-stripped procedure; procedure for nanocrystal film deposition and SEM images of the nanocrystal films; absorbance change of NR and NPL films at different elapsed times during reduction/oxidation; electrochemical kinetics study of NR and NPL films during Li insertion/deinsertion by chronoamperometry; chronopotentiometry of NR and NPL films; DFT calculations using VASP, table for comparison of lattice parameters and table for comparison of Bader electronic chargers on niobium sites in different lithiated structures (PDF)

AUTHOR INFORMATION

Corresponding Authors

Graeme Henkelman − *Department of Chemistry and Oden Institute for Computational Engineering and Sciences, The University of Texas at Austin, Austin, Texas 78712-0165, United States;* orcid.org/0000-0002-0336-7153; Email: henkelman@utexas.edu

Delia J. Milliron − *McKetta Department of Chemical Engineering, The University of Texas at Austin, Austin, Texas 78712-1589, United States;* orcid.org/0000-0002-8737-451X; Email: milliron@che.utexas.edu

Authors

Hsin-Che Lu − *McKetta Department of Chemical Engineering, The University of Texas at Austin, Austin, Texas 78712-1589, United States;* orcid.org/0000-0001-5673-2647

Naman Katyal − *Department of Chemistry and Oden Institute for Computational Engineering and Sciences, The University of Texas at Austin, Austin, Texas 78712-0165, United States*

Complete contact information is available at: https://pubs.acs.org/10.1021/jacs.1c06901

Author Contributions

[§]H.-C.L. and N.K. contributed equally to this work.

Notes

The authors declare no competing financial interest.

ACKNOWLEDGMENTS

The authors acknowledge support from CBMM, the National Science Foundation (Grant CHE-1905263), the Robert A. Welch Foundation (Grants F-1848 and F-1841), and the Texas Advanced Computing Center and XSEDE (Grant TG-CHE190010) for computational resources.

REFERENCES

(1) Wang, Y.; Runnerstrom, E. L.; Milliron, D. J. Switchable Materials for Smart Windows. *Annu. Rev. Chem. Biomol. Eng.* **2016**, *7*, 283−304.

(2) Runnerstrom, E. L.; Llordés, A.; Lounis, S. D.; Milliron, D. J. Nanostructured Electrochromic Smart Windows: Traditional Materials and NIR-selective Plasmonic Nanocrystals. *Chem. Commun.* **2014**, *50*, 10555−10572.

(3) Dahlman, C. J.; Tan, Y.; Marcus, M. A.; Milliron, D. J. Spectroelectrochemical Signatures of Capacitive Charging and Ion Insertion in Doped Anatase Titania Nanocrystals. *J. Am. Chem. Soc.* **2015**, *137*, 9160−9166.

(4) Lu, H.-C.; Ghosh, S.; Katyal, N.; Lakhanpal, V. S.; Gearba-Dolocan, I. R.; Henkelman, G.; Milliron, D. J. Synthesis and Dual-Mode Electrochromism of Anisotropic Monoclinic $Nb_{12}O_{29}$ Colloidal Nanoplatelets. *ACS Nano* **2020**, *14*, 10068−10082.

(5) Zhang, S.; Cao, S.; Zhang, T.; Lee, J. Y. Plasmonic Oxygen-Deficient TiO_{2-x} Nanocrystals for Dual-Band Electrochromic Smart Windows with Efficient Energy Recycling. *Adv. Mater.* **2020**, *32*, 2004686.

(6) Kim, J.; Ong, G. K.; Wang, Y.; LeBlanc, G.; Williams, T. E.; Mattox, T. M.; Helms, B. A.; Milliron, D. J. Nanocomposite Architecture for Rapid, Spectrally-Selective Electrochromic Modulation of Solar Transmittance. *Nano Lett.* **2015**, *15*, 5574−5579.

(7) Ozkan, E.; Lee, S.-H.; Tracy, C. E.; Pitts, J. R.; Deb, S. K. Comparison of Electrochromic Amorphous and Crystalline Tungsten Oxide Films. *Sol. Energy Mater. Sol. Cells* **2003**, *79*, 439−448.

(8) Schmitt, M.; Heusing, S.; Aegerter, M. A.; Pawlicka, A.; Avellaneda, C. Electrochromic Properties of Nb_2O_5 Sol−Gel Coatings. *Sol. Energy Mater. Sol. Cells* **1998**, *54*, 9−17.

(9) Niklasson, G. A.; Granqvist, C. G. Electrochromics for Smart Windows: Thin Films of Tungsten Oxide and Nickel Oxide, and Devices based on These. *J. Mater. Chem.* **2007**, *17*, 127−156.

(10) Triana, C. A.; Granqvist, C. G.; Niklasson, G. A. Electrochromism and Small-Polaron Hopping in Oxygen Deficient and Lithium Intercalated Amorphous Tungsten Oxide Films. *J. Appl. Phys.* **2015**, *118*, 024901.

(11) Özer, N.; Rubin, M. D.; Lampert, C. M. Optical and Electrochemical Characteristics of Niobium Oxide Films Prepared by Sol-gel Process and Magnetron Sputtering A Comparison. *Sol. Energy Mater. Sol. Cells* **1996**, *40*, 285−296.

(12) Besnardiere, J.; Ma, B.; Torres-Pardo, A.; Wallez, G.; Kabbour, H.; González-Calbet, J. M.; Von Bardeleben, H. J.; Fleury, B.; Buissette, V.; Sanchez, C.; Le Mercier, T.; Cassaignon, S.; Portehault, D. Structure and Electrochromism of Two-Dimensional Octahedral Molecular Sieve h'-WO3. *Nat. Commun.* **2019**, *10*, 327.

(13) Heo, S.; Dahlman, C. J.; Staller, C. M.; Jiang, T.; Dolocan, A.; Korgel, B. A.; Milliron, D. J. Enhanced Coloration Efficiency of Electrochromic Tungsten Oxide Nanorods by Site Selective Occupation of Sodium Ions. *Nano Lett.* **2020**, *20*, 2072−2079.

(14) Heo, S.; Kim, J.; Ong, G. K.; Milliron, D. J. Template-Free Mesoporous Electrochromic Films on Flexible Substrates from Tungsten Oxide Nanorods. *Nano Lett.* **2017**, *17*, 5756−5761.

(15) Heo, S.; Cho, S. H.; Dahlman, C. J.; Agrawal, A.; Milliron, D. J. Influence of Crystalline and Shape Anisotropy on Electrochromic Modulation in Doped Semiconductor Nanocrystals. *ACS Energy Lett.* **2020**, *5*, 2662−2670.

(16) De Trizio, L.; Buonsanti, R.; Schimpf, A. M.; Llordes, A.; Gamelin, D. R.; Simonutti, R.; Milliron, D. J. Nb-Doped Colloidal TiO_2 Nanocrystals with Tunable Infrared Absorption. *Chem. Mater.* **2013**, *25*, 3383−3390.

(17) Balaji, S.; Djaoued, Y.; Albert, A.-S.; Ferguson, R. Z.; Brüning, R. Hexagonal Tungsten Oxide Based Electrochromic Devices: Spectroscopic Evidence for the Li Ion Occupancy of Four-Coordinated Square Windows. *Chem. Mater.* **2009**, *21*, 1381−1389.

(18) Evans, R. C.; Austin, R.; Miller, R. C.; Preston, A.; Nilsson, Z. N.; Ma, K.; Sambur, J. B. Surface-Facet-Dependent Electrochromic Properties of WO_3 Nanorod Thin Films: Implications for Smart Windows. *ACS Appl. Nano Mater.* **2021**, *4*, 3750−3759.

(19) Kim, J.; Agrawal, A.; Krieg, F.; Bergerud, A.; Milliron, D. J. The Interplay of Shape and Crystalline Anisotropies in Plasmonic Semiconductor Nanocrystals. *Nano Lett.* **2016**, *16*, 3879−3884.

(20) Agrawal, A.; Kriegel, I.; Milliron, D. J. Shape-Dependent Field Enhancement and Plasmon Resonance of Oxide Nanocrystals. *J. Phys. Chem. C* **2015**, *119*, 6227−6238.

(21) Schmitt, M.; Aegerter, M. A. Electrochromic Properties of Pure and Doped Nb_2O_5 Coatings and Devices. *Electrochim. Acta* **2001**, *46*, 2105−2111.

(22) Macek, M.; Orel, B.; Krasovec, U. O. The Effect of Lithiation on the Electrochromism of Sol-gel Derived Niobium Oxide Films. *J. Electrochem. Soc.* **1997**, *144*, 3002−3010.

(23) Ong, G. K.; Saez Cabezas, C. A.; Dominguez, M. N.; Skjærvø, S. L.; Heo, S.; Milliron, D. J. Electrochromic Niobium Oxide Nanorods. *Chem. Mater.* **2020**, *32*, 468−475.

(24) Yao, D. D.; Rani, R. A.; O'Mullane, A. P.; Kalantar-zadeh, K.; Ou, J. Z. High Performance Electrochromic Devices Based on Anodized Nanoporous Nb_2O_5. *J. Phys. Chem. C* **2014**, *118*, 476−481.

(25) Griffith, K. J.; Wiaderek, K. M.; Cibin, G.; Marbella, L. E.; Grey, C. P. Niobium Tungsten Oxides for High-Rate Lithium-Ion Energy Storage. *Nature* **2018**, *559*, 556−563.

(26) Koçer, C. P.; Griffith, K. J.; Grey, C. P.; Morris, A. J. Lithium Diffusion in Niobium Tungsten Oxide Shear Structures. *Chem. Mater.* **2020**, *32*, 3980−3989.

(27) Griffith, K. J.; Seymour, I. D.; Hope, M. A.; Butala, M. M.; Lamontagne, L. K.; Preefer, M. B.; Koçer, C. P.; Henkelman, G.; Morris, A. J.; Cliffe, M. J.; Dutton, S. E.; Grey, C. P. Ionic and Electronic Conduction in $TiNb_2O_7$. *J. Am. Chem. Soc.* **2019**, *141*, 16706−16725.

(28) Preefer, M. B.; Saber, M.; Wei, Q.; Bashian, N. H.; Bocarsly, J. D.; Zhang, W.; Lee, G.; Milam-Guerrero, J.; Howard, E. S.; Vincent, R. C.; Melot, B. C.; Van der Ven, A.; Seshadri, R.; Dunn, B. S. Multielectron Redox and Insulator-to-Metal Transition upon Lithium Insertion in the Fast-Charging, Wadsley-Roth Phase PNb_9O_{25}. *Chem. Mater.* **2020**, *32*, 4553−4563.

(29) Griffith, K. J.; Forse, A. C.; Griffin, J. M.; Grey, C. P. High-Rate Intercalation without Nanostructuring in Metastable Nb_2O_5 Bronze Phases. *J. Am. Chem. Soc.* **2016**, *138*, 8888−8899.

(30) Li, Y.; Sun, C.; Goodenough, J. B. Electrochemical Lithium Intercalation in Monoclinic $Nb_{12}O_{29}$. *Chem. Mater.* **2011**, *23*, 2292−2294.

(31) Cava, R. J.; Batlogg, B.; Krajewski, J. J.; Poulsen, H. F.; Gammel, P.; Peck, W. F.; Rupp, L. W. Electrical and Magnetic Properties of $Nb_2O_{5-\delta}$ Crystallographic Shear Structures. *Phys. Rev. B: Condens. Matter Mater. Phys.* **1991**, *44*, 6973−6981.

(32) Koçer, C. P.; Griffith, K. J.; Grey, C. P.; Morris, A. J. First-Principles Study of Localized and Delocalized Electronic States in Crystallographic Shear Phases of Niobium Oxide. *Phys. Rev. B: Condens. Matter Mater. Phys.* **2019**, *99*, 075151.

(33) Pattathil, P.; Giannuzzi, R.; Manca, M. Self-Powered NIR-Selective Dynamic Windows Based on Broad Tuning of the Localized Surface Plasmon Resonance in Mesoporous ITO Electrodes. *Nano Energy* **2016**, *30*, 242−251.

(34) Pattathil, P.; Scarfiello, R.; Giannuzzi, R.; Veramonti, G.; Sibillano, T.; Qualtieri, A.; Giannini, C.; Cozzoli, P. D.; Manca, M. Near-Infrared Selective Dynamic Windows Controlled by Charge Transfer Impedance at the Counter Electrode. *Nanoscale* **2016**, *8* (48), 20056−20065.

(35) Barawi, M.; De Trizio, L.; Giannuzzi, R.; Veramonti, G.; Manna, L.; Manca, M. Dual Band Electrochromic Devices Based on Nb-Doped TiO_2 Nanocrystalline Electrodes. *ACS Nano* **2017**, *11* (4), 3576−3584.

(36) Barawi, M.; Veramonti, G.; Epifani, M.; Giannuzzi, R.; Sibillano, T.; Giannini, C.; Rougier, A.; Manca, M. A Dual Band Electrochromic Device Switchable Across Four Distinct Optical Modes. *J. Mater. Chem. A* **2018**, *6* (22), 10201−10205.

(37) Brown, P. J.; Fox, A. G.; Maslen, E. N.; O'Keefe, M. A.; Willis, B. T. M. Intensity of diffracted intensities. In *International Tables for Crystallography*, 1st ed.; Prince, E., Ed.; Springer: Dordrecht, The

https://doi.org/10.1021/jacs.1c06901
J. Am. Chem. Soc. 2021, 143, 15745−15755

Netherlands, 2006; Vol. C, pp 554−595, DOI: 10.1107/97809553602060000600.
(38) Momma, K.; Izumi, F. VESTA: A Three-Dimensional Visualization System for Electronic and Structural Analysis. *J. Appl. Crystallogr.* **2008**, *41* (3), 653−658.
(39) Kresse, G.; Furthmüller, J. Efficient Iterative Schemes for Ab Initio Total-Energy Calculations Using A Plane-Wave Basis Set. *Phys. Rev. B: Condens. Matter Mater. Phys.* **1996**, *54*, 11169−11186.
(40) Perdew, J. P.; Burke, K.; Ernzerhof, M. Generalized Gradient Approximation Made Simple. *Phys. Rev. Lett.* **1996**, *77*, 3865−3868.
(41) Ong, S. P.; Richards, W. D.; Jain, A.; Hautier, G.; Kocher, M.; Cholia, S.; Gunter, D.; Chevrier, V. L.; Persson, K. A.; Ceder, G. Python Materials Genomics (Pymatgen): A Robust, Open-Source Python Library for Materials Analysis. *Comput. Mater. Sci.* **2013**, *68*, 314−319.
(42) Gajdoš, M.; Hummer, K.; Kresse, G.; Furthmüller, J.; Bechstedt, F. Linear Optical Properties in the Projector-Augmented Wave Methodology. *Phys. Rev. B: Condens. Matter Mater. Phys.* **2006**, *73*, 045112.
(43) Henkelman, G.; Arnaldsson, A.; Jónsson, H. A Fast and Robust Algorithm for Bader Decomposition of Charge Density. *Comput. Mater. Sci.* **2006**, *36*, 354−360.
(44) Ali, R. F.; Nazemi, A. H.; Gates, B. D. Surfactant Controlled Growth of Niobium Oxide Nanorods. *Cryst. Growth Des.* **2017**, *17*, 4637−4646.
(45) Gordon, T. R.; Cargnello, M.; Paik, T.; Mangolini, F.; Weber, R. T.; Fornasiero, P.; Murray, C. B. Nonaqueous Synthesis of TiO_2 Nanocrystals Using TiF_4 to Engineer Morphology, Oxygen Vacancy Concentration, and Photocatalytic Activity. *J. Am. Chem. Soc.* **2012**, *134*, 6751−6761.
(46) Nakajima, K.; Hirata, J.; Kim, M.; Gupta, N. K.; Murayama, T.; Yoshida, A.; Hiyoshi, N.; Fukuoka, A.; Ueda, W. Facile Formation of Lactic Acid from a Triose Sugar in Water over Niobium Oxide with a Deformed Orthorhombic Phase. *ACS Catal.* **2018**, *8*, 283−290.
(47) Murayama, T.; Chen, J.; Hirata, J.; Matsumoto, K.; Ueda, W. Hydrothermal Synthesis of Octahedra-Based Layered Niobium Oxide and Its Catalytic Activity as a Solid Acid. *Catal. Sci. Technol.* **2014**, *4*, 4250−4257.
(48) Zhao, Y.; Eley, C.; Hu, J.; Foord, J. S.; Ye, L.; He, H.; Tsang, S. C. E. Shape-Dependent Acidity and Photocatalytic Activity of Nb_2O_5 Nanocrystals with an Active TT (001) Surface. *Angew. Chem., Int. Ed.* **2012**, *51*, 3846−3849.
(49) Li, B.; Gu, M.; Nie, Z.; Wei, X.; Wang, C.; Sprenkle, V.; Wang, W. Nanorod Niobium Oxide as Powerful Catalysts for an All Vanadium Redox Flow Battery. *Nano Lett.* **2014**, *14*, 158−165.
(50) Buonsanti, R.; Grillo, V.; Carlino, E.; Giannini, C.; Kipp, T.; Cingolani, R.; Cozzoli, P. D. Nonhydrolytic Synthesis of High-Quality Anisotropically Shaped Brookite TiO_2 Nanocrystals. *J. Am. Chem. Soc.* **2008**, *130*, 11223−11233.
(51) Bronstein, L. M.; Huang, X.; Retrum, J.; Schmucker, A.; Pink, M.; Stein, B. D.; Dragnea, B. Influence of Iron Oleate Complex Structure on Iron Oxide Nanoparticle Formation. *Chem. Mater.* **2007**, *19*, 3624−3632.
(52) Llordés, A.; Wang, Y.; Fernandez-Martinez, A.; Xiao, P.; Lee, T.; Poulain, A.; Zandi, O.; Saez Cabezas, C. A.; Henkelman, G.; Milliron, D. J. Linear Topology in Amorphous Metal Oxide Electrochromic Networks Obtained via Low-Temperature Solution Processing. *Nat. Mater.* **2016**, *15*, 1267.
(53) McConnell, A. A.; Aderson, J. S.; Rao, C. N. R. Raman Spectra of Niobium Oxides. *Spectrochim. Acta* **1976**, *32*, 1067−1076.
(54) Dong, A.; Ye, X.; Chen, J.; Kang, Y.; Gordon, T.; Kikkawa, J. M.; Murray, C. B. A Generalized Ligand-Exchange Strategy Enabling Sequential Surface Functionalization of Colloidal Nanocrystals. *J. Am. Chem. Soc.* **2011**, *133*, 998−1006.
(55) Yoshimura, K.; Miki, T.; Iwama, S.; Tanemura, S. Characterization of Niobium Oxide Electrochromic Thin Films Prepared by Reactive D.C. Magnetron Sputtering. *Thin Solid Films* **1996**, *281*−*282*, 235−238.
(56) Berggren, L.; Jonsson, J. C.; Niklasson, G. A. Optical Absorption in Lithiated Tungsten Oxide Thin Films: Experiment and Theory. *J. Appl. Phys.* **2007**, *102*, 083538.
(57) Ederth, J.; Hoel, A.; Niklasson, G. A.; Granqvist, C. G. Small Polaron Formation in Porous WO_{3-x} Nanoparticle Films. *J. Appl. Phys.* **2004**, *96*, 5722−5726.
(58) Augustyn, V.; Come, J.; Lowe, M. A.; Kim, J. W.; Taberna, P.-L.; Tolbert, S. H.; Abruña, H. D.; Simon, P.; Dunn, B. High-rate Electrochemical Energy Storage through Li^+ Intercalation Pseudocapacitance. *Nat. Mater.* **2013**, *12*, 518.
(59) Kim, J. W.; Augustyn, V.; Dunn, B. The Effect of Crystallinity on the Rapid Pseudocapacitive Response of Nb_2O_5. *Adv. Eng. Mater.* **2012**, *2*, 141−148.
(60) Liang, L.; Zhang, J.; Zhou, Y.; Xie, J.; Zhang, X.; Guan, M.; Pan, B.; Xie, Y. High-Performance Flexible Electrochromic Device Based on Facile Semiconductor-to-Metal Transition Realized by $WO_3{\cdot}2H_2O$ Ultrathin Nanosheets. *Sci. Rep.* **2013**, *3*, 1936.
(61) Li, M.; Gould, T.; Su, Z.; Li, S.; Pan, F.; Zhang, S. Electrochromic Properties of $Li_4Ti_5O_{12}$: From Visible to Infrared Spectrum. *Appl. Phys. Lett.* **2019**, *115*, 073902.
(62) He, Y.; Li, T.; Zhong, X.; Zhou, M.; Dong, G.; Diao, X. Lattice and Electronic Structure Variations in Critical Lithium Doped Nickel Oxide Thin Film for Superior Anode Electrochromism. *Electrochim. Acta* **2019**, *316*, 143−151.
(63) Waldron, J. E. L.; Green, M. A.; Neumann, D. A. Structure and Electronic Properties of Monoclinic $Nb_{12}O_{29}$. *J. Phys. Chem. Solids* **2004**, *65*, 79−86.
(64) Ohsawa, T.; Okubo, J.; Suzuki, T.; Kumigashira, H.; Oshima, M.; Hitosugi, T. An n-Type Transparent Conducting Oxide: $Nb_{12}O_{29}$. *J. Phys. Chem. C* **2011**, *115*, 16625−16629.
(65) Cava, R. J.; Batlogg, B.; Krajewski, J. J.; Gammel, P.; Poulsen, H. F.; Peck, W. F.; Rupp, L. W. Antiferromagnetism and Metallic Conductivity in $Nb_{12}O_{29}$. *Nature* **1991**, *350*, 598−600.
(66) Lappas, A.; Waldron, J. E. L.; Green, M. A.; Prassides, K. Magnetic Ordering in the Charge-Ordered $Nb_{12}O_{29}$. *Phys. Rev. B: Condens. Matter Mater. Phys.* **2002**, *65*, 134405.
(67) Llunell, M.; Alemany, P.; Canadell, E. Crystal Structure and Coexistence of Localized and Delocalized Electrons in $Nb_{12}O_{29}$. *J. Solid State Chem.* **2000**, *149*, 176−179.
(68) Waldron, J. E. L.; Green, M. A.; Neumann, D. A. Charge and Spin Ordering in Monoclinic $Nb_{12}O_{29}$. *J. Am. Chem. Soc.* **2001**, *123*, 5833−5834.
(69) Fang, C. M.; van Huis, M. A.; Xu, Q.; Cava, R. J.; Zandbergen, H. W. Unexpected Origin of Magnetism in Monoclinic $Nb_{12}O_{29}$ from First-Principles Calculations. *J. Mater. Chem. C* **2015**, *3*, 651−657.